


Bandwidth enhancement in damping control for piezoelectric nanopositioning stages with load uncertainty: Design and implementation

Journal of Vibration and Control
2021, Vol. 27(11–12) 1382–1394
© The Author(s) 2020
Article reuse guidelines:
sagepub.com/journals-permissions
DOI: 10.1177/1077546320941705
journals.sagepub.com/home/jvc


Jie Ling¹ , Zhao Feng¹ , Xi Kang² and Xiaohui Xiao¹

Abstract

High bandwidth and fast tracking of desired trajectories are eagerly required in various applications that use piezoelectric nanopositioning stages, especially in atomic force microscopes where the vibration stemming from lightly damped modes of stages is a challenging control problem. In this study, a bandwidth-enhanced positive acceleration, velocity, and position feedback damping controller is presented to achieve the tracking bandwidth exceeding the first resonant frequency through using a novel pole-shift method. The stability of the positive feedback damped loop is examined by a mixed passivity, small-gain approach, and Nyquist theorem framework. Also, in conjunction with a proportional–integral tracking controller, robust stability is addressed for load uncertainties. Experimental application to a piezoelectric nanopositioning stage demonstrates that a closed-loop bandwidth of 282.5 Hz is achieved, which exceeds the dominating resonance of the stage at 210 Hz. The achieved bandwidth is 1.35 times larger than the dominating resonance, which is a competitive result among most existing damping control approaches. Comparative tracking results verify the effectiveness of the proposed control scheme on the suppression of low-frequency hysteresis and tracking performance of high-speed triangular waves under load variations.

Keywords

Piezoelectric nanopositioning stage, damping control, stability analysis, high-speed tracking, load uncertainty

1. Introduction

The piezoelectric nanopositioning stage becomes a crucial component to achieve nanometer positioning resolution, high stiffness, and fast response time by using piezoelectric actuators and flexure-hinge-guided mechanisms (Feng et al., 2017; Yong et al., 2012) and has been widely applied in scientific and industrial fields at nanoscale, such as scanning probe microscopes (Devasia et al., 2007; Salapaka and Salapaka, 2008), atomic force microscopes (AFMs) (Rana et al., 2016), micromanipulation systems (Li et al., 2019), ultraprecision machine tools (Wu and Xu, 2018), wafer stages (Evers et al., 2019), energy harvester (Lu et al., 2020) and so on. Recently, these systems such as AFMs for video-rate imaging (Yong et al., 2013) that require high-speed motion have posed new challenges on high-bandwidth and precision tracking of piezoelectric nanopositioning stages. However, the inherent hysteresis nonlinearities and vibrations caused by the lightly damped resonant dynamics of these stages limit the improvement of the tracking performance (Gu et al., 2014).

To compensate for hysteresis nonlinearity–caused error effectively, model-based feedforward control methods are the most common approaches via constructing inverse hysteresis models (Cao and Chen, 2015; Rakotondrabe, 2017; Sabarianand et al., 2020). Various models such as Preisach model (Liu et al., 2012), Bouc–Wen model (Habineza et al., 2015), and Maxwell resistive capacitor model (Liu et al., 2014; Shan et al., 2016) have been adopted to mitigate hysteresis. It should be noted that lots of parameters should be identified to improve modeling accuracy. Alternatively, to simplify the controller design, the

¹School of Power and Mechanical Engineering, Wuhan University, China

²Department of Biomedical Engineering, National University of Singapore, Singapore

Received: 9 April 2020; accepted: 22 June 2020

Corresponding author:

Jie Ling, Hubei Key Laboratory of Waterjet Theory and New Technology, Wuhan University, 8 South Donghu Road, Wuhan 430072, China.
Email: jie.ling.whu@outlook.com

overall complex model of piezoelectric nanopositioning stages are composed of the static hysteresis and linear part (Gu et al., 2015), and the high-gain feedback controllers can improve low-frequency tracking performance significantly (Ling et al., 2020). However, as the motion speed increases, the performance is degraded severely for the lightly damped modes (Eielsen et al., 2013; Habineza et al., 2017; Verbaan et al., 2017).

Traditionally, the built-in integral or proportional–integral (PI) controllers are commonly used in commercial piezoelectric nanopositioning stages for the ease of implementation, but the closed-loop bandwidth is restricted within 2% of the first resonance frequency of the stages (Yong et al., 2012). To push the improvement of tracking bandwidth, some general feedback control strategies are reported to improve the tracking performance during high-speed motion, such as robust control (Habibullah et al., 2019; Kang et al., 2020; Shahabi et al., 2020), adaptive control (Ling et al., 2019; Zhang et al., 2017), sliding mode control (Xu, 2017) and so on. Also, for periodic signals, repetitive controllers can provide the required performance for the signal generator wrapped in this control scheme (Li et al., 2016b). However, the implementation of these high-order controllers in practical applications may require advanced digital signal process systems.

Alternatively, low-order negative-imaginary (NI) damping controllers can increase the damping ratio of resonant modes effectively and provide sufficient robustness for systems with collocated position sensors such as nanopositioners (Petersen, 2016; Petersen and Lanzon, 2010). These controllers, such as integral resonant control (Bhikkaji and Moheimani, 2008; Namavar et al., 2013), positive position feedback control (Aphale et al., 2008; Mahmood and Moheimani, 2009), modified positive velocity and position feedback control (San-Millan et al., 2015), resonant control (RC) (Das et al., 2015), and polynomial-based control (Namavar and Aphale, 2014) provide fixed structures and lower computational complexity, which makes them simple in design and implementation. Note that these NI damping controllers are elaborately designed for the typical second-order models, which are usual NI systems. Therefore, the positive feedback stability can be described as that where the dc loop gain is less than unity as the model and the controller are both NI with one of them being strictly NI (Lanzon and Petersen, 2008; Petersen, 2016).

However, in practical piezoelectric nanopositioning stages, the identified model according to the data collected from position sensors may not be NI because of the delay in sensors or actuators (Das et al., 2014b). As a result, the above stability criteria are not suitable. In addition, the controller parameters are so conservative that resulting in a low gain of the controller and lower closed-loop bandwidth through small-gain theorem that requires the loop gain to be less than 1 in the overall frequency intervals (Skogestad and Postlethwaite, 2007). To overcome the drawbacks, a mixed NI and small-gain approach was

proposed to demonstrate the stability (Patra and Lanzon, 2011) and applied to design an RC for the piezoelectric tube scanner (Das et al., 2014b). Moreover, a mixed passivity, NI, and small-gain approach was used for a passive damping controller design (Das et al., 2014a). Furthermore, the positive acceleration, velocity, and position feedback (PAVPF) damping controller was used to realize the arbitrary closed-loop poles for a third-order transfer function (Li et al., 2017). It should be noted that although the tracking bandwidth is improved significantly via implementing these methods, the closed-loop bandwidth is still less than the first resonant frequency of the stages.

The study is motivated to achieve the tracking bandwidth exceeding the first resonant frequency of the piezoelectric nanopositioning stages with load uncertainty. Inspired by the existing pole shift technique in Namavar and Aphale (2014), a novel pole placement method is proposed to shift the resonant frequency. Differences between the methods in Namavar and Aphale (2014) and this work lie in: (1) a second-order system is focused in Namavar and Aphale (2014), which is extended into a third-order system in this work; (2) stability analysis is not included in Namavar and Aphale (2014), which is accomplished using a mixed passivity, small gain, and Nyquist stability criterion in this work; (3) a nominal system and simulation results are discussed in Namavar and Aphale (2014), which are extended to an actual platform with load uncertainty and experimental results in this work.

Thus, the method in this work can be regarded as an extension from the work in Namavar and Aphale (2014) with more practicability and applicability for bandwidth enhancement of fixed-order damping controllers in Bhikkaji and Moheimani (2008), Namavar et al. (2013), Aphale et al. (2008), San-Millan et al. (2015), Mahmood and Moheimani (2009) and Das et al. (2015). Using the proposed pole placement method, a bandwidth-enhanced positive acceleration, velocity, and position feedback (BEPVPF) damping controller is then designed to enhance the bandwidth substantially. Compared with the existing PAVPF control in Li et al. (2017), the tracking bandwidth is notably improved. Comprehensive experiments based on a nanopositioning stage with load uncertainty were conducted to evaluate the designed damping controller. Herein, the main contribution of this study is twofold:

1. A bandwidth enhancement damping method is proposed for piezoelectric nanopositioning stages to make the closed-loop bandwidth surpass the first resonant frequency;
2. A mixed passivity, small gain, and Nyquist stability criterion is proposed to analyze the stability and robust stability of the designed controller under load variations.

The rest of the article is organized as follows. In Section 2, the system setup is described in detail. The controller design

of the BEPAVPF damping controller in tandem with PI tracking controller and the relevant stability analysis are presented in Section 3. Section 4 gives detailed controller implementation and analysis. Experiments results on a piezoelectric nanopositioning stage and comparisons with different controllers are elaborated in Section 5, and Section 6 gives the conclusions.

2. System description

2.1. Experimental setup

The experimental setup is shown in Figure 1. A piezoelectric nanopositioning stage (model: P-561.3CD from Physik Instrumente) is developed, and the x axis is used to evaluate the performance. The control input voltage is generated by 16-bit digital-to-analog converters via the data acquisition card PCI 6289 of National Instruments Corporation and subsequently amplified by a piezo amplifier module (model: E-503.00 from Physik Instrumente) with an output range of 0–100 V for the piezoelectric nanopositioning stage. The output position normalized as 0–10 V and read via a sensor monitor (model: E-509.C3A from Physik Instrumente) is passed to the data acquisition card PCI 6289 by 18-bit analog-to-digital converters. The overall control system is built in Simulink real-time environment on the host computer and executed real time on the target computer. In this study, the sample frequency of the system is set to 10 kHz.

2.2. System identification

A sine-sweep input between 0.1 Hz and 500 Hz is applied to the x axis to identify the linear dynamic model of the piezoelectric nanopositioning stage. By using the system identification toolbox in MATLAB, the nominal continuous transfer function without load $G_n(s)$ with the Laplace operator s can be identified as

$$G_n(s) = \frac{12.41s^2 - 1.568 \times 10^5 s + 4.074 \times 10^5}{s^3 + 441.7s^2 + 1.762 \times 10^5 s + 6.818 \times 10^5} \quad (1)$$

In terms of robustness, another challenge of the stage is that the first resonant mode frequency varied with the load on it. Figure 2 shows the frequency responses as the mass on the stage increasing from 0 g to 300 g. The variation of the resonance frequency of the stage is evident from 210 Hz to 190 Hz. The sensitivity to load may result in the unstable closed-loop system. Therefore, the control objective of this study is to design a low-order damping controller to achieve the closed-loop bandwidth exceeding the first resonant frequency and remain robust to uncertainties caused by the loads for the third-order system.

3. Controller design

3.1. Bandwidth-enhanced PAVPF damping control

To improve the tracking bandwidth, a BEPAVPF damping control is developed as Figure 3, where the plant $G_n(s)$ and damping controller $C_d(s)$ are connected with positive feedback. $u(t)$ is the input of the damped loop, and $y(t)$ denotes the position output of the system. For the ease of calculation in the following section, the third-order plant $G_n(s)$ is expressed with known parameters as

$$G_n(s) = \frac{n_2 s^2 + n_1 s + n_0}{s^3 + d_2 s^2 + d_1 s + d_0} \quad (2)$$

where n_2 , n_1 , n_0 , d_2 , d_1 , and d_0 are the nominal parameters of the system.

To enhance the closed-loop bandwidth and damp the resonant mode, the output of BEPAVPF damping controller is the synthesis of acceleration, velocity, and position signals based on the system output (Das et al., 2014a). The transfer function of the controller can be described as

$$C_d(s) = \frac{n_{e2}s^2 + n_{e1}s + n_{e0}}{s^2 + d_{e1}s + d_{e0}} \quad (3)$$

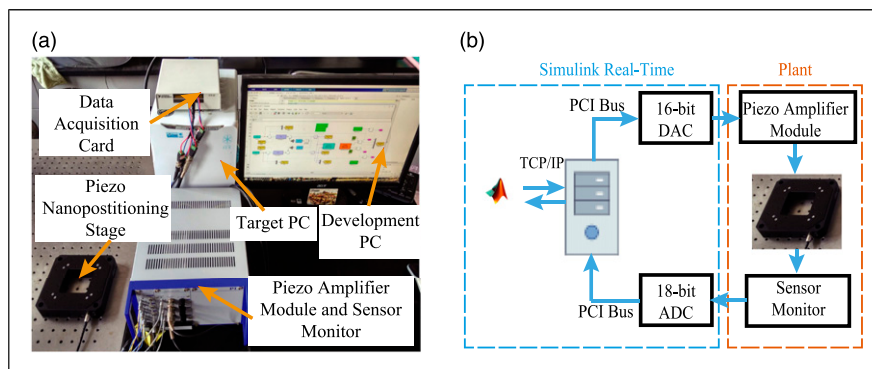


Figure 1. Experimental setup of the piezoelectric nanopositioning stage. (a) Experimental platform. (b) Block diagram of the control system.

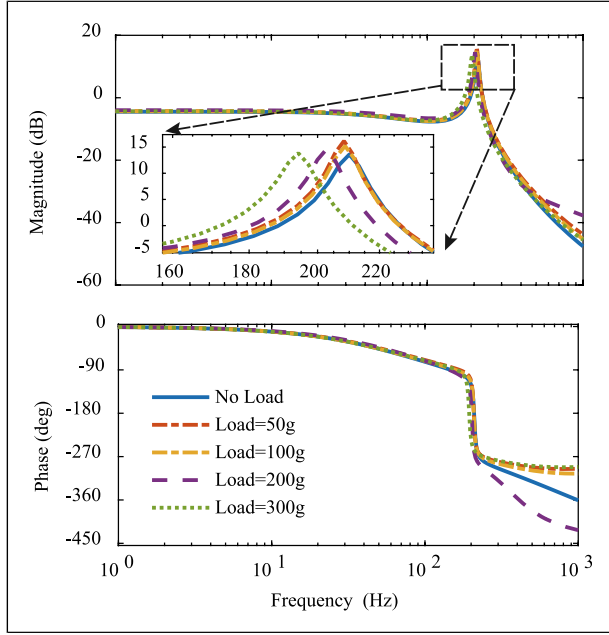


Figure 2. Open-loop frequency responses of the piezoelectric nanopositioning stage with different loads.

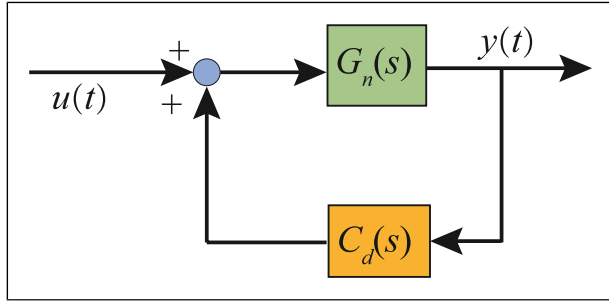


Figure 3. Block diagram of the system with bandwidth-enhanced positive acceleration, velocity, and position feedback damping controller through positive feedback.

where n_{c2} , n_{c1} , n_{c0} , d_{c1} , and d_{c0} are the parameters to be calculated in the following content. According to the block diagram in Figure 3, the damped loop transfer function from control input $u(t)$ to output displacement $y(t)$ can be written as

$$G_d(s) = \frac{G_n(s)}{1 - G_n(s)C_d(s)} \quad (4)$$

Substituting equations (2) and (3) into (4), it can be deduced that the poles of $G_d(s)$ are the roots of the polynomial

$$P(s) = (s^3 + d_2s^2 + d_1s + d_0)(s^2 + d_{c1}s + d_{c0}) - (n_2s^2 + n_1s + n_0)(n_{c2}s^2 + n_{c1}s + n_{c0}) \quad (5)$$

Then, equation (5) can be expanded as a five-order polynomial

$$\begin{aligned} P(s) = & s^5 + (d_{c1} + d_2 - n_2n_{c2})s^4 \\ & + (d_1 + d_{c0} + d_2d_{c1} - n_2n_{c1} - n_1n_{c2})s^3 \\ & + (d_2d_{c0} + d_1d_{c1} + d_0 - n_2n_{c0} - n_1n_{c1} - n_0n_{c2})s^2 \\ & + (d_1d_{c0} + d_0d_{c1} - n_1n_{c0} - n_0n_{c1})s \\ & + (d_0d_{c0} - n_0n_{c0}) \end{aligned} \quad (6)$$

To enhance the tracking bandwidth and damp the resonance, the desired poles of $G_d(s)$ should be allocated elaborately to achieve the anticipated performance. Assume that $\{p_d^j\}_j^5$ are the desired pole positions of the closed-loop system and for the proposed BEPAVPF damping controller in this study, they are given by

$$\begin{aligned} p_d^1 &= \alpha(\text{Re}(p_G) + \text{Im}(p_G)i) \\ p_d^2 &= \alpha(\text{Re}(p_G) - \text{Im}(p_G)i) \\ p_d^3 &= \alpha\beta \text{Re}(p_G) + \alpha \text{Im}(p_G)i \\ p_d^4 &= \alpha\beta \text{Re}(p_G) - \alpha \text{Im}(p_G)i \\ p_d^5 &= \gamma \end{aligned} \quad (7)$$

where $\text{Re}(p_G)$ and $\text{Im}(p_G)$ represent the real part and imaginary part of the complex poles in the third-order transfer function equation (2). α , β , and γ are the parameters to be designed with $\alpha > 1$, $\beta > 1$, and $\gamma < 0$.

It should be mentioned that for the traditional method, the desired poles are placed to make only the real part further away from the imaginary axis, that is $\alpha = 1$, $\beta > 1$, and $p_d^1 = p_d^3$, $p_d^2 = p_d^4$. Figure 4 demonstrates the different desired locations of the damped-loop poles. This kind of damping controllers can be found in Mahmood and Moheimani (2009) and Li et al. (2017) to damp the resonance. However, the resonant frequency of the damped transfer function is still nearly unaltered in comparison with the original open-loop resonance so that the tracking bandwidth remains less than the original first resonant frequency. In this study, the first pair of desired complex poles is moved along the constant damping ratio line to push the resonant frequency to be α times greater than the original. Based on that, the second pair of desired complex poles is allocated to make the real part β times larger than the first pair of poles. The third pole is located in the negative-real axis with γ distance. The proposed pole placement can shift a higher resonant frequency and damp the resonance at the same time to achieve bandwidth-enhanced performance.

To obtain the controller parameters, the characteristic equation of the damped loop with desired poles can be given as

$$\begin{aligned} Q(s) &= (s - p_d^1)(s - p_d^2)(s - p_d^3)(s - p_d^4)(s - p_d^5) \\ &= s^5 + K_4s^4 + K_3s^3 + K_2s^2 + K_1s + K_0 \end{aligned} \quad (8)$$

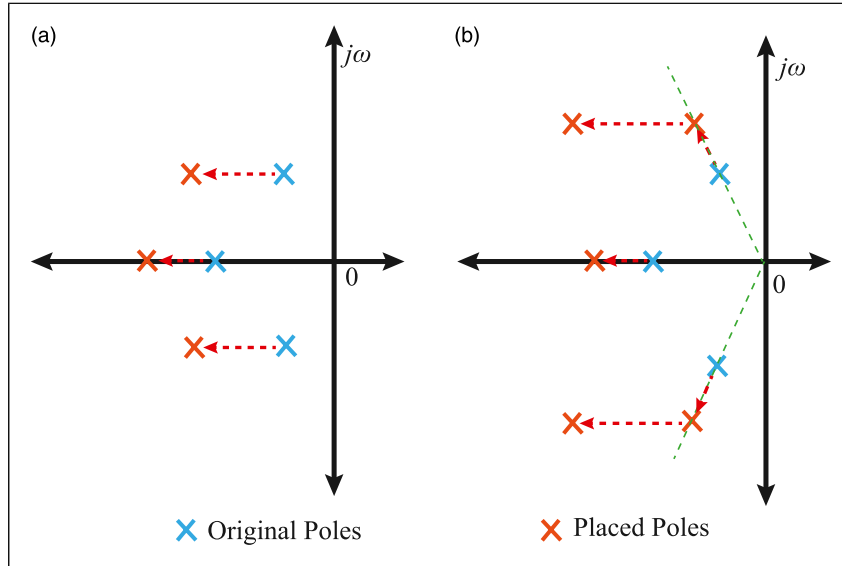


Figure 4. Schematic diagram of different desired locations of the damped-loop poles. (a) The traditional method. (b) The proposed method.

where

$$\begin{aligned}
 K_4 &= -2\alpha(1+\beta)\text{Re}(p_G) - \gamma \\
 K_3 &= (\alpha^2 + 2\text{Im}(p_G)^2 + \alpha^2\beta^2 + 4\text{Re}(p_G)^2\beta)\alpha^2 \\
 &\quad + 2\text{Re}(p_G)\alpha\gamma(1+\beta) \\
 K_2 &= -2\text{Re}(p_G)\alpha^3(\alpha^2\beta^2 + \text{Im}(p_G)^2 + \text{Re}(p_G)^2\beta) \\
 &\quad + \beta\text{Im}(p_G)^2 - 2\text{Re}(p_G)\alpha\gamma(1+\beta) + 2\text{Re}(p_G)\alpha\beta \\
 K_1 &= 2\text{Re}(p_G)\alpha^3\gamma(\alpha^2\beta^2 + \text{Im}(p_G)^2 + \text{Re}(p_G)^2\beta + \beta\text{Im}(p_G)^2) \\
 &\quad + \alpha^4(\text{Re}(p_G)^2 + \text{Im}(p_G)^2)(\text{Re}(p_G)^2\beta^2 + \text{Im}(p_G)^2) \\
 K_0 &= -\alpha^4\gamma(\text{Re}(p_G)^2 + \text{Im}(p_G)^2)(\text{Re}(p_G)^2\beta^2 + \text{Im}(p_G)^2)
 \end{aligned} \quad (9)$$

To determine the desired poles of the damped system with BEPAVPF, the coefficients of equation (8) should match those of equation (6), that is

$$\begin{aligned}
 K_4 &= d_{c1} + d_2 - n_2n_{c2} \\
 K_3 &= d_1 + d_{c0} + d_2d_{c1} - n_2n_{c1} - n_1n_{c2} \\
 K_2 &= d_2d_{c0} + d_1d_{c1} + d_0 - n_2n_{c0} - n_1n_{c1} - n_0n_{c2} \\
 K_1 &= d_1d_{c0} + d_0d_{c1} - n_1n_{c0} - n_0n_{c1} \\
 K_0 &= d_0d_{c0} - n_0n_{c0}
 \end{aligned} \quad (10)$$

Note that the above equations can be written in the matrix form as

$$Ax = b \quad (11)$$

where

$$A = \begin{bmatrix} 1 & 0 & -n_2 & 0 & 0 \\ d_2 & 1 & -n_1 & -a_2 & 0 \\ d_1 & d_2 & -n_0 & -n_1 & -n_2 \\ d_0 & d_1 & 0 & -n_0 & n_1 \\ 0 & d_0 & 0 & 0 & -n_0 \end{bmatrix} \quad (12)$$

$$x = [d_{c1} \quad d_{c0} \quad n_{c2} \quad n_{c1} \quad n_{c0}]^T \quad (13)$$

$$b = [K_4 - d_2 \quad K_3 - d_1 \quad K_2 - d_0 \quad K_1 \quad K_0]^T \quad (14)$$

Combining equations (10)–(14), the parameters can be calculated.

3.2. Stability analysis

Stability of the proposed controller can be analyzed through the mixed passivity, small-gain, and Nyquist stability criterion by dividing different frequency-dependent intervals. Considering a single-input single-output real rational stable transfer function $M(s)$, the definition of passive, negative passivity, and finite-gain properties are given below.

Definition 1 (Petersen and Lanzon, 2010). The stable system $M(s)$ is said to be passive for all ω frequencies such that $s = j\omega$ is not a pole of $M(s)$ if it follows that

$$M(j\omega) + M^*(j\omega) \geq 0 \quad (15)$$

where $M^*(j\omega)$ is the complex conjugate transpose of $M(j\omega)$. From the Nyquist plot, equation (16) is also which the phase of $M(j\omega)$ satisfies

$$\angle M(j\omega) \in [-\pi/2, \pi/2] \quad (16)$$

Definition 2 (Petersen and Lanzon, 2010). The stable system $M(s)$ is said to be of negative passivity for all ω frequencies such that $s = j\omega$ is not a pole of $M(s)$ if it follows that

$$-M(j\omega) - M^*(j\omega) \geq 0 \quad (17)$$

Equation (17) is also which the phase of $M(j\omega)$ satisfies

$$\angle M(j\omega) \in [\pi/2, 3\pi/2] \quad (18)$$

Definition 3 (Das et al., 2014a). The stable system $M(s)$ is said to be finite-gain system bounded by a gain k with $0 \leq k < \infty$ if

$$k = \inf \left\{ \bar{k} : -M(j\omega)M^*(j\omega) + \bar{k}^2 \geq 0 \right\} \quad (19)$$

for all ω , where \bar{k} stands for the upper bound of the gain k .

To analysis the stability of the controller as shown in Figure 3, the frequency intervals with different properties are described as:

1. Let ψ_P be frequency intervals $[\omega_1, \omega_2]$ with $0 < \omega_1 \leq \omega_2$, where $G_n(s)$ satisfies the passive property and $C_d(s)$ satisfies the negative-passivity property or vice versa.
2. Let ψ_{FG} be frequency intervals $[\omega_3, \omega_4]$ with $0 \leq \omega_3 \leq \omega_4$, where $G_n(s)$ is finite-gain bounded by a gain k_1 and $C_d(s)$ is finite-gain bounded by a gain k_2 with $k_1 k_2 < 1$.
3. Let ψ_N be frequency intervals $[\omega_5, \omega_6]$ with $0 \leq \omega_5 \leq \omega_6$, where either $G_n(s)$ or $C_d(s)$ satisfies the above two conditions.

Theorem 1. Consider the strictly proper stable transfer function $G_n(s)$ and stable proper $C_d(s)$ with relative degree 0 and the two systems are connected as in Figure 3, where $\psi_P \cup \psi_{FG} \cup \psi_N = [0, \infty)$ denotes the overall positive frequency set. For $k_1 > |G_n(0)|$ and $k_2 > |C_d(0)|$, if the positive feedback interconnection is stable, it follows that

$$k_1 k_2 < 1 \quad (20)$$

and in the frequency interval ψ_N , $Re(G_n(j\omega)C_d(j\omega)) = 1$ has no solution, or

$$\prod_{i=1}^m Im(G_n(j\omega_i)C_d(j\omega_i)) > 0 \quad (21)$$

where $w_i \in \{1, 2, \dots, m\}$ are satisfied with $Re(G_n(j\omega_i) \times C_d(j\omega_i)) = 1$.

Proof 1. The above theorem can be proved by three dependent triplets, that is ψ_P , ψ_{FG} , and ψ_N .

1. For $\omega \in \psi_P$ according to Definition 1 and Definition 2, the phases of $G_n(s)$ and $C_d(s)$ satisfy $\angle G_n(j\omega) \in [-\pi/2, \pi/2]$ and $\angle C_d(j\omega) \in [\pi/2, 3\pi/2]$ respectively, where $G_n(s)$ is passive and $C_d(s)$ is of negative passivity. With the positive feedback of the two systems, it can be equivalent to negative feedback, where both

$G_n(s)$ and $-C_d(s)$ are passive. Therefore, the phase of $-G_n(s)C_d(s)$ will be $\angle G_n(j\omega) C_d(j\omega) \in [0, \pi]$ and its Nyquist plot cannot intersect the negative real axis. Consequently, $-G_n(s) C_d(s)$ will not encircle $(-1, 0)$ and satisfy the Nyquist stability criterion. A similar result can be deduced when $G_n(s)$ is negative passive and $C_d(s)$ is passive.

2. For $\omega \in \psi_{FG}$, according to Definition 3, there exist k_1 and k_2 so that $|G_n(s)|^2 < k_1^2$ and $|C_d(s)|^2 < k_2^2$. Hence, taking small-gain theorem and $|G_n(s) C_d(s)| < k_1 k_2$ into consideration, the feedback of $G_n(s)$ and $C_d(s)$ is stable if and only if $k_1 k_2 < 1$ with $k_1 > |G_n(0)|$ and $k_2 > |C_d(0)|$.
3. For $\omega \in \psi_N$, neither the passivity theorem nor small-gain theorem can determine the stability. According to the Nyquist stability criterion, if the Nyquist plot lies in the left plane of $V(j\omega)$ with $Re(V(j\omega)) = 1$, it will not encircle $(1, 0)$, so $Re(G_n(j\omega) C_d(j\omega)) = 1$ should have no solution. If $\prod_{i=1}^m Im(G_n(j\omega_i)C_d(j\omega_i)) = 0$ exists for ω_i , the Nyquist plot should pass the point $(1, 0)$, resulting in the unstable closed-loop system; if $\prod_{i=1}^m Im(G_n(j\omega_i)C_d(j\omega_i)) < 0$, the Nyquist plot must intersect the positive real axis, which will make the plot encircle $(1, 0)$ for $\lim_{\omega \rightarrow \infty} G_n(j\omega)C_d(j\omega) = 0$. Therefore, equation (21) is satisfied. This concludes the proof of Theorem 1.

It should be noted that $C_d(s)$ is not a strictly proper transfer function, $\lim_{\omega \rightarrow \infty} C_d(j\omega)$ is not zero with high-pass property. The gain of $C_d(s)$ may be not bounded by the finite-gain k_2 . As a result, the stability analysis in Patra and Lanzon (2011) and Li et al. (2017) is not suitable for the proposed BEPAVPF damping controller because of the requirement of $\lim_{\omega \rightarrow \infty} C_d(j\omega) = 0$. In this study, the stability at high-frequency interval $\omega \in \psi_N$ is determined by equation (21).

3.3. Tracking controller design and stability

In this study, the proposed BEPAVPF controller is designed to extend the tracking bandwidth and damp the resonance. To address the static low-frequency hysteresis nonlinearity and improve the robust ability to model uncertainties, a PI controller is adopted in the outer feedback loop, as shown in Figure 5, where $\Delta(s)$ is the transfer function of multiplicative uncertainty of the system, $r(t)$ is the reference signal, $v(t)$ and $d(t)$ are the input and output signals of $\Delta(s)$ respectively. $C_t(s)$ is the PI tracking controller expressed as

$$C_t(s) = k_p + \frac{k_i}{s} \quad (22)$$

where k_p and k_i are the proportional gain and integral gain, respectively. It is well known that an accurate model is usually difficult to obtain.

The stability of the positive feedback interconnection between $G_n(s)$ and $C_d(s)$ is given in Theorem 1. To give the

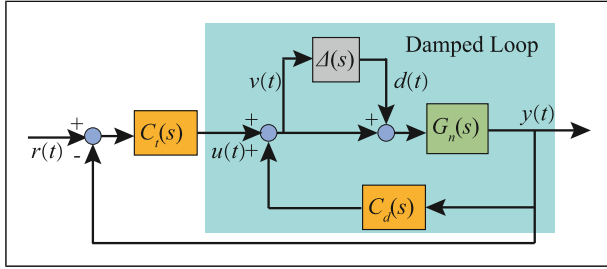


Figure 5. Block diagram of the overall control scheme of the system with uncertainties.

overall stability of the system with the tracking controller $C_t(s)$, Theorem 2 is introduced as follows.

Theorem 2. If the parameters in $C_d(s)$ satisfy Theorem 1, the stability of the closed-loop system with tracking controller $C_t(s)$ is given by

$$\|G_n(s)(C_t(s) - C_d(s))\|_\infty < 1 \quad (23)$$

Proof 2. According to the transfer function of the controller equation (4), the closed-loop transfer function with $C_t(s)$ can be expressed as

$$T(s) = \frac{C_t(s)G_n(s)}{1 + G_n(s)(C_t(s) - C_d(s))} \quad (24)$$

Therefore, based on the small-gain theorem, the closed-loop stability can be expressed as equation (23). This concludes the proof of Theorem 2.

Moreover, the load on the piezoelectric nanopositioning stage can result in the variation of the resonance so that it is crucial to analyze the robust stability of the overall closed-loop system.

Theorem 3. Let the actual plant be described as $G(s) = (1 + \Delta(s))G_n(s)$, where $\Delta(s)$ is the multiplicative model uncertainty. Assume that the damping control $C_d(s)$ and tracking controller $C_t(s)$ can stabilize the closed loop for $G_n(s)$. The robust stability of the closed-loop system is given by

$$\left\| \frac{G_n(s)(C_d(s) - C_t(s))}{1 - G_n(s)(C_d(s) - C_t(s))} \Delta(s) \right\|_\infty < 1 \quad (25)$$

Proof 3. According to Figure 5, the transfer function from $d(t)$ to $v(t)$ is derived as

$$T_\Delta(s) = \frac{G_n(s)(C_d(s) - C_t(s))}{1 - G_n(s)(C_d(s) - C_t(s))} \quad (26)$$

Therefore, the control scheme in Figure 5 for internal robust analysis can be reformulated as shown in Figure 6.

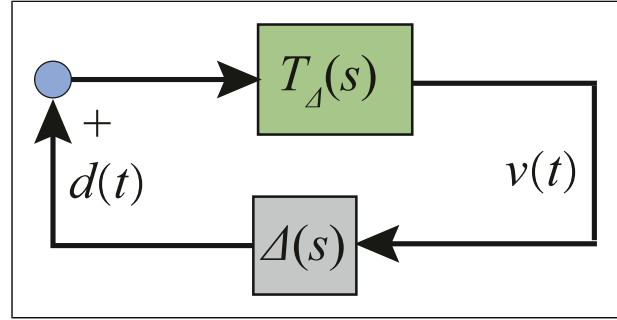


Figure 6. Reformulation of block diagram for robust stability analysis.

Based on the small-gain theorem, the condition for robust stability can be deduced as

$$\|T_\Delta(s)\Delta(s)\|_\infty < 1 \quad (27)$$

This concludes the proof of Theorem 3.

Remark 1. In this study, we should emphasize Theorem 1 for proving the stability of damping loop (the main contribution), Theorem 2 for closed-loop stability, and Theorem 3 for robust stability.

4. Controller implementation

4.1. Implementation of the damping controller

For the piezoelectric nanopositioning stage described in Section 2, the BEPAVPF damping controller is designed first to extend the bandwidth. Based on the equations (10)–(14), the calculated damping controller with $\alpha = 1.45$, $\beta = 40$ and $\gamma = -800$ is given by

$$C_d(s) = \frac{-23s^2 - 1.969 \times 10^4 s - 1.843 \times 10^7}{s^2 + 1520s + 1.271 \times 10^7} \quad (28)$$

To analysis the stability of the positive connection between $G_n(s)$ and $C_d(s)$, the finite gains are chosen as $k_1 = 0.61 > |G_n(0)| = 0.597$ and $k_2 = 1.62 > |C_d(0)| = 1.449$ that satisfy $k_1 k_2 = 0.9882 < 1$. Figure 7 demonstrates the frequency intervals with different properties. It is clear that in the frequency intervals $[0, 921.8]$ rad/s and $[3363.9, 5970]$ rad/s, $G_n(s)$ has passive property whereas $C_d(s)$ has negative-passivity property, which is contained in ψ_P . $G_n(s)$ and $C_d(s)$ are bounded by k_1 and k_2 respectively, in the frequency intervals $[921.8, 948.8]$ rad/s, which satisfies ψ_{FG} . In the frequency intervals $[941.8, 1419.1]$ rad/s, $G_n(s)$ has passive property whereas $C_d(s)$ has negative-passivity property, which is contained in ψ_N . The remaining intervals $[1419.1, 3363.9]$ rad/s and $[5970, \infty]$ rad/s compose the ψ_N , which meets the condition of equation (21) from the

Nyquist plot in Figure 7(c). Therefore, in the overall frequency interval, Theorem 1 is satisfied for equations (1) and (28).

In terms of the frequency domain, Figure 8 shows the comparisons between open-loop transfer function and the system with traditional PAVPF and proposed BEPAVPF.

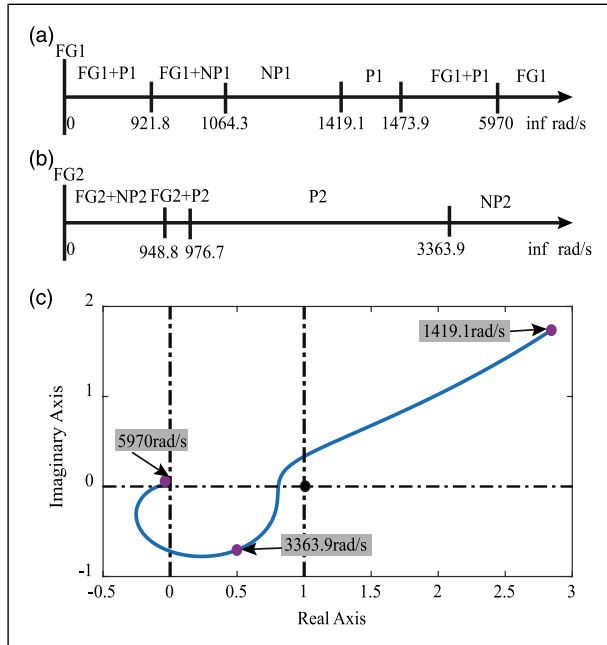


Figure 7. Frequency intervals for stability analysis of the proposed bandwidth-enhanced positive acceleration, velocity, and position feedback (FG: finite-gain property, P: passive property, and NP: negative-passivity property). (a) Frequency intervals of $G_n(s)$. (b) Frequency intervals of $C_d(s)$. (c) Nyquist plot of $G_n(s)C_d(s)$ for ψ_N .

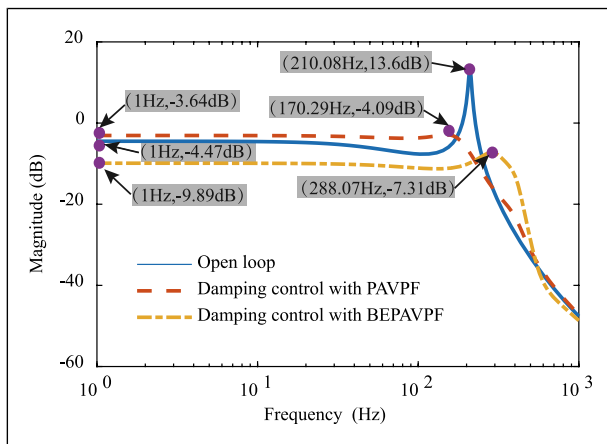


Figure 8. Frequency responses of the system in open loop, with PAVPF and with BEPAVPF. PAVPF: positive acceleration, velocity, and position feedback; BEPAVPF: bandwidth-enhanced positive acceleration, velocity, and position feedback.

The damped loop with BEPAVPF shifts the resonance to 288.07 Hz, which is far beyond the original at 210.08 Hz. Moreover, the resonant gain is damped from 18.07 dB for open loop to 2.58 dB. Although the PAVPF achieves a small resonant gain of 0.38 dB, the resonant frequency is merely 170.29 Hz.

4.2. Implementation of the tracking controller

For the tracking control gains, they can be preliminarily initialized based on Theorems 2 and 3. The robust stability condition can be verified through simulation cases. Subsequently, considering that the actual experimental platform suffers from the inevitable uncertainties, the parameters can be tuned and determined elaborately and carefully by an iterative trial and error method to get the proper anticipated performance for each specified controller in the experiments. This ensures that the comparisons of outcomes achieved are suitably fair, as each specified controller has essentially been appropriately and properly tuned.

Finally, in this work, the gains of tracking controllers are given as $k_p = 0.001$, $k_i = 172.89$ for PI, $k_p = 0.336$, $k_i = 432$ for the traditional PAVPF, and $k_p = 0.95751$, $k_i = 1389.45$ for the proposed BEPAVPF.

4.3. Closed-loop responses in time and frequency domain

To compare the achieved closed-loop responses (i.e. rising time, overshoot, bandwidth, and frequency characteristics) of the PI, PI + PAVPF, and PI + BEPAVPF, time and frequency domain responses are depicted in Figures 9–11.

4.3.1. Step responses. As shown in Figure 9, it can be seen that all the three closed-loop schemes are better than open loop in terms of steady state errors. However, owing to the limited bandwidth of the PI control alone, the rising time is

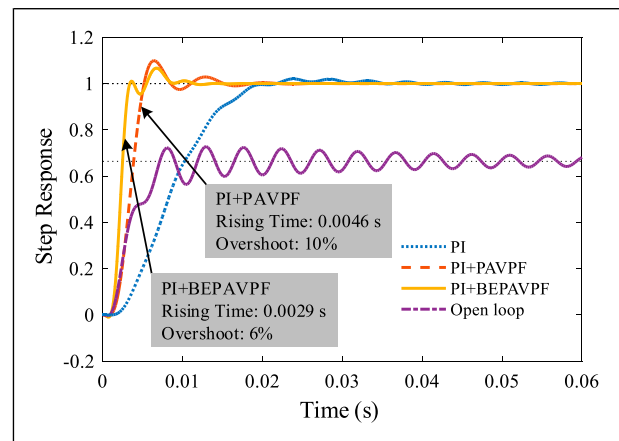


Figure 9. Step responses of the system with the three controllers.

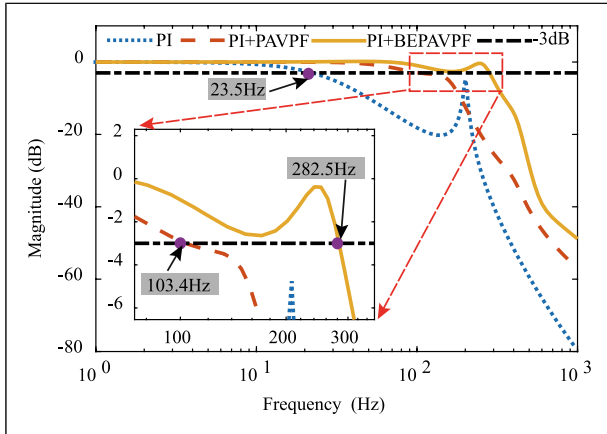


Figure 10. Closed-loop frequency responses of the system with different controllers.

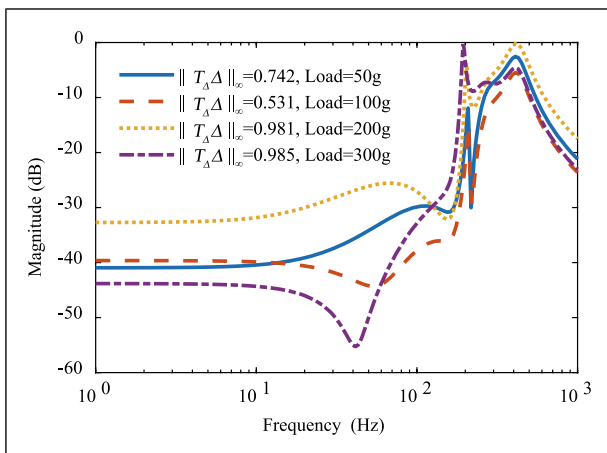


Figure 11. Robust stability of the proposed controller with different loads.

obviously larger than PI + PAVPF, and PI + BEPAVPF. In addition, the designed PI + BEPAVPF achieves a rising time of 2.9 ms which makes an improvement of 37% from that of PI+PAVPF. The overshoots of PI + PAVPF and PI + BEPAVPF are 10% and 6%, respectively. Herein, the results of step responses indicate that the designed PI + BEPAVPF obtains smaller rising time and overshoot than the traditional PI + PAVPF.

4.3.2. Frequency responses. According to Figure 10, the commonly used PI controller has the lowest bandwidth of 23.5 Hz, and the proposed method achieves 282.5 Hz bandwidth, which is 1.732 times more than PI + PAVPF with 103.4 Hz and exceeds the open-loop resonant frequency at 210.08 Hz. Moreover, bode diagrams of $T_{\Delta}(s)$ with different loads varying from 50 g to 300 g are illustrated in Figure 11, the maximal $\|T_{\Delta}(s)\|_{\infty}$ is $0.985 < 1$, which satisfies Theorem 3.

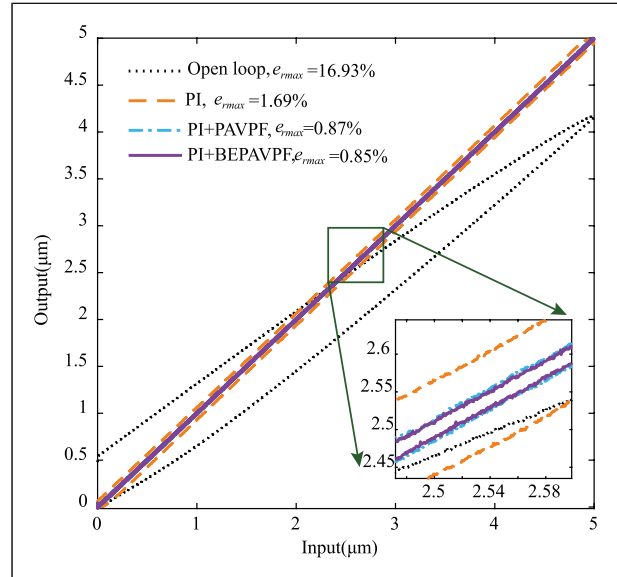


Figure 12. Experimental results of hysteresis suppression with different controllers. Tracking performance of high-speed triangular waves.

5 Experimental result

5.1. Suppression of low frequency hysteresis

In this study, the hysteresis nonlinearity is treated as a low-frequency external disturbance without building hysteresis modeling for simple implementation. Experimental results of hysteresis curves with different controllers are displayed in Figure 12 when a 1 Hz triangular wave with 5 μm peak-to-peak amplitude is injected into x axis. For open-loop tracking, the relative maximal error ($e_{r\max}$) is 16.93%, which exhibits evident hysteresis nonlinearity. Although the standalone PI controller can suppress hysteresis partly, the $e_{r\max}$ of 1.39% is still large for precision tracking. The PI + PAVPF and PI + BEPAVPF have similar results, that is 0.87% and 0.85% respectively, which demonstrates that the low-frequency hysteresis is mitigated substantially.

5.2. Tracking performance of high speed triangular waves

To validate the high-speed tracking performance of the proposed method, the triangular waves widely used in AFMs as references of the fast motion axis for raster scanning are performed on the piezoelectric nanopositioning stage.

5.2.1. Tracking results without load. To compare the tracking performance of the PI, PI + PAVPF, and PI + BEPAVPF controllers, Figure 13 shows the experimental results as references with different frequencies input at 5 Hz, 10 Hz, 25 Hz, and 50 Hz. The root-mean-square errors (e_{rms}) and maximal errors (e_{\max}) are tabulated in Table 1 in detail. It can

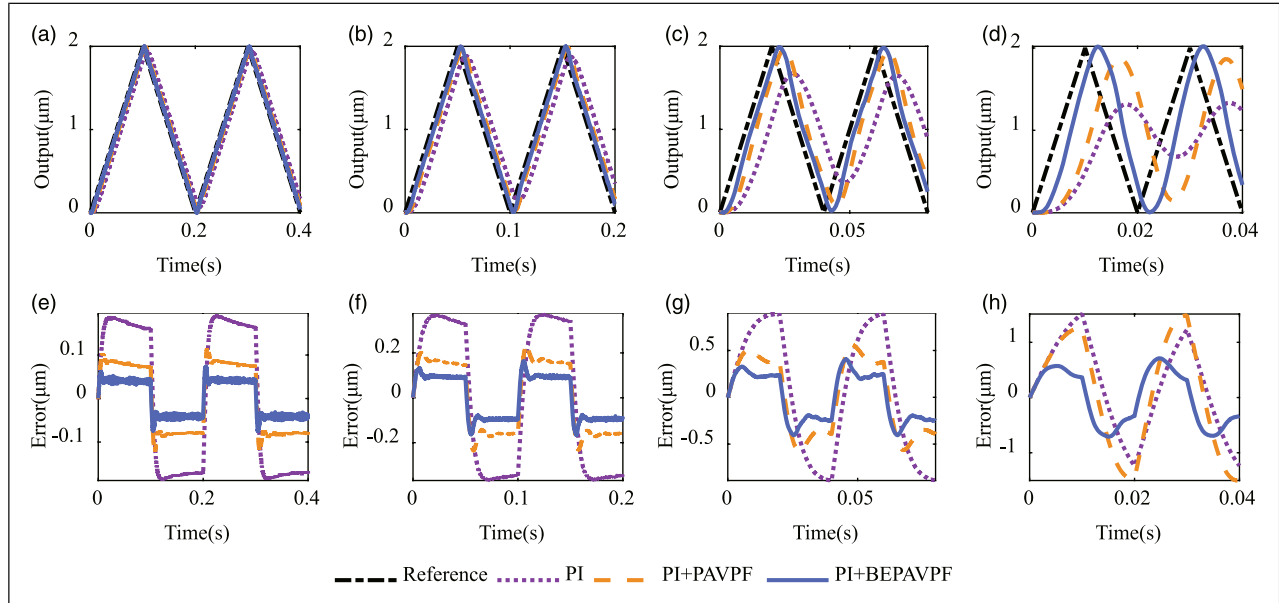


Figure 13. Experimental results of different controllers without load. (a) Tracking results at 5 Hz. (b) Tracking results at 10 Hz. (c) Tracking results at 25 Hz. (d) Tracking results at 50 Hz. (e) Tracking errors at 5 Hz. (f) Tracking errors at 10 Hz. (g) Tracking errors at 25 Hz. (h) Tracking errors at 50 Hz.

be seen that both PI+PAVPF and PI + BEPAVPF controllers significantly improve the tracking performance compared with the PI control. With the frequency of input reference increasing, the tracking performance of the PI controller is severely degraded for the limited bandwidth. As an illustration, the experimental results with 25 Hz triangular waves are discussed. The performances of PI + PAVPF and PI + BEPAVPF improve 39.58%, 61.47% for e_{rms} and 35.55%, 54.33% for e_{max} respectively, in comparison with PI controller. Besides, it can be found that the proposed PI + BEPAVPF also demonstrates better performance than PI + PAVPF with the errors reducing by 36.23% and 29.14% in terms of e_{rms} and e_{max} . A similar conclusion can also be made from the other references as displayed in Table 1.

Remark 2. It can be observed from Figure 13 that the errors increase in high-frequency tracking cases. The main reason for the proposed PI + BEPAVPF scheme lies in the increased phase lag instead of the nonlinearity effect. The phase lag is resulted from the limited bandwidth as the 50 Hz raster scanning is relatively high for the used platform in this study. However, in the AFM scanning applications, perfectly delayed tracking is better than imperfect timely tracking for which the phase lags of the recorded system outputs fixed upon the controllers are designed (Li et al., 2016a). To compare the tracking performances of different controllers, the phase lags can be removed using some post-processing techniques as equation (21) in Ling et al. (2019). In this study, we did not shift the curves using equation (21) in Ling et al. (2019), as even before shifting, the proposed

Table 1. Statistical results of tracking errors with different references (unit: μm).

Error (μm)		PI	PI + PAVPF	PI + BEPAVPF
5 Hz	e_{rms}	0.168	0.081	0.042
	e_{max}	0.194	0.121	0.074
10 Hz	e_{rms}	0.323	0.163	0.156
	e_{max}	0.373	0.236	0.166
25 Hz	e_{rms}	0.667	0.403	0.257
	e_{max}	0.889	0.573	0.406
50 Hz	e_{rms}	0.838	1.003	0.492
	e_{max}	1.512	1.502	0.710

PI: proportional-integral; PAVPF: positive acceleration, velocity, and position feedback; BEPAVPF: bandwidth-enhanced positive acceleration, velocity, and position feedback.

PI + BEPAVPF scheme can perform the best among the three control schemes.

5.2.2. Tracking results with loads. As depicted in Figure 2, different loads make the first resonance shift from 210 Hz to 190 Hz. Therefore, in this subsection, the 25 Hz triangular signals are fed into the closed-loop system with different controllers to test the robust stability. Note that the proposed controller in this study is designed for the unloaded model and its parameters remain unchanged during the experiments. The tracking performance with different loads is plotted in Figure 14, and the statistical results of errors are recorded in Table 2. It is evident that the proposed

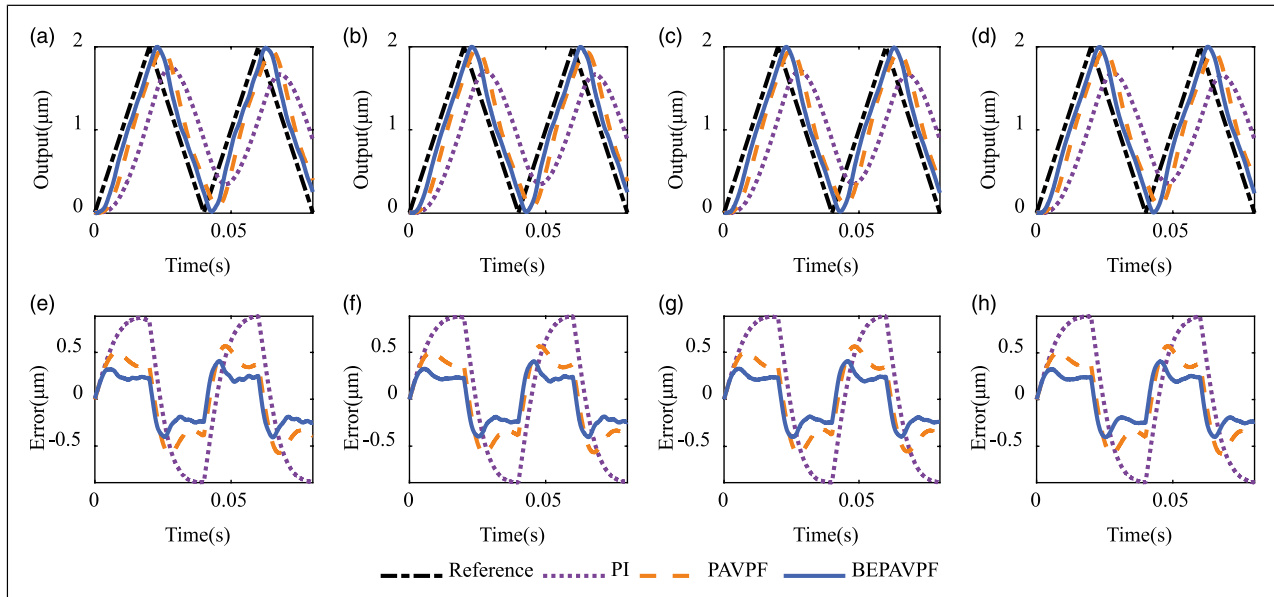


Figure 14. Experimental results of different controllers with loads. (a) Tracking results at 50 g load. (b) Tracking results at 100 g load. (c) Tracking results at 200 g load. (d) Tracking results at 500 g load. (e) Tracking errors at 50 g load. (f) Tracking errors at 100 g load. (g) Tracking errors at 200 g load. (h) Tracking errors at 300 g load.

Table 2. Statistical results of tracking errors with different loads (unit: μm).

Error (μm)		PI	PI + PAVPF	PI + BEPAVPF
50 g	e_{rms}	0.672	0.399	0.256
	e_{max}	0.891	0.582	0.409
100 g	e_{rms}	0.671	0.399	0.255
	e_{max}	0.888	0.578	0.404
200 g	e_{rms}	0.671	0.396	0.255
	e_{max}	0.884	0.578	0.405
300 g	e_{rms}	0.668	0.402	0.258
	e_{max}	0.892	0.579	0.408

PI: proportional–integral; PAVPF: positive acceleration, velocity, and position feedback; BEPAVPF: bandwidth-enhanced positive acceleration, velocity, and position feedback.

PI + BEPAVPF damping controller achieves the best performance compared with PI and PI + PAVPF controllers for each load. For the PI + BEPAVPF, the e_{rms} varies between 0.255 μm and 0.258 μm and the e_{max} varies between 0.404 μm and 0.409 μm . The relative change rates are less than 0.39% and 0.74% in comparison with the statistical error without load, which demonstrates that the proposed method is not sensitive to the model variation and obtains sufficient robustness to uncertainties.

6. Conclusion

In this study, the BEPAVPF damping controller for a third-order piezoelectric nanopositioning stage is developed to push

the resonant frequency to a substantially higher frequency and damp the corresponding resonance through a novel pole placement method to achieve bandwidth exceeding the first resonant frequency. Through integrating with a high-gain PI tracking controller, the tracking performance is enhanced further. The stability of the positive connection between the plant and BEPAVPF is analyzed via a mixed passivity, small-gain approach, and Nyquist theorem. The robust stability condition of the overall scheme is also derived in this study to handle load uncertainties. Experimental tracking results of triangular waves under different scenarios are given to evaluate the performance of the proposed control approach in comparison with PI controller and traditional PAVPF control scheme. Hence, this study provides a solution to break through the inherent limitation of the lightly damped modes of a piezoelectric nanopositioner for high-speed raster scanning.

The future work will take the effect of rate-dependent hysteresis nonlinearity into consideration, especially for the large stroke motion of the stage.

Declaration of conflicting interests

The author(s) declared no potential conflicts of interest with respect to the research, authorship, and/or publication of this article.

Funding

The author(s) disclosed receipt of the following financial support for the research, authorship, and/or publication of this article: This work was supported by the Project funded by China Postdoctoral Science Foundation under Grant No. 2018M642907, Shenzhen Science and Technology Program under Grant No. JCYJ20170306171514468 and Natural Science Foundation of China under Grant No. 51375349.

ORCID iDs

Jie Ling  <https://orcid.org/0000-0002-6786-0422>

Zhao Feng  <https://orcid.org/0000-0001-7213-9413>

References

- Aphale SS, Devasia S and Reza Moheimani SO (2008) High-bandwidth control of a piezoelectric nanopositioning stage in the presence of plant uncertainties. *Nanotechnology* 19(12): 125503.
- Bhikkaji B and Moheimani SR (2008) Integral resonant control of a piezoelectric tube actuator for fast nanoscale positioning. *IEEE/ASME Transactions on mechatronics* 13(5): 530–537.
- Cao Y and Chen X (2015) A survey of modeling and control issues for piezo-electric actuators. *Journal of Dynamic Systems, Measurement, and Control* 137(1): 014001.
- Das SK, Pota HR and Petersen IR (2014a) Damping controller design for nanopositioners: a mixed passivity, negativeimaginary, and small-gain approach. *IEEE/ASME Transactions on Mechatronics* 20(1): 416–426.
- Das SK, Pota HR and Petersen IR (2014b) Resonant controller design for a piezoelectric tube scanner: a mixed negativeimaginary and small-gain approach. *IEEE Transactions on Control Systems Technology* 22(5): 1899–1906.
- Das SK, Pota HR and Petersen IR (2015) Multivariable negativeimaginary controller design for damping and cross coupling reduction of nanopositioners: a reference model matching approach. *IEEE/ASME Transactions on Mechatronics* 20(6): 3123–3134.
- Devasia S, Eleftheriou E and Moheimani SR (2007) A survey of control issues in nanopositioning. *IEEE Transactions on Control Systems Technology* 15(5): 802–823.
- Eielsen AA, Vagia M, Gravdahl JT, et al. (2013) Damping and tracking control schemes for nanopositioning. *IEEE/ASME Transactions on Mechatronics* 19(2): 432–444.
- Evers E, van de Wal M and Oomen T (2019) Beyond decentralized wafer/reticle stage control design: a double-youla approach for enhancing synchronized motion. *Control Engineering Practice* 83: 21–32.
- Feng Z, Ling J, Ming M, et al. (2017) High-bandwidth and flexible tracking control for precision motion with application to a piezo nanopositioner. *Review of Scientific Instruments* 88(8): 085107.
- Gu GY, Li CX, Zhu LM, et al. (2015) Modeling and identification of piezoelectric-actuated stages cascading hysteresis nonlinearity with linear dynamics. *IEEE/ASME Transactions on Mechatronics* 21(3): 1792–1797.
- Gu GY, Zhu LM, Su CY, et al. (2014) Modeling and control of piezo-actuated nanopositioning stages: a survey. *IEEE Transactions on Automation Science and Engineering* 13(1): 313–332.
- Habibullah H, Pota HR and Petersen I (2019) A robust control approach for high-speed nanopositioning applications. *Sensors and Actuators A: Physical* 292: 137–148.
- Habineza D, Rakotondrabe M and Le Gorrec Y (2015) Boucwen modeling and feedforward control of multivariable hysteresis in piezoelectric systems: application to a 3-dof piezotube scanner. *IEEE Transactions on Control Systems Technology* 23(5): 1797–1806.
- Habineza D, Zouari M, Le Gorrec Y, et al. (2017) Multivariable compensation of hysteresis, creep, badly damped vibration, and cross couplings in multiaxes piezoelectric actuators. *IEEE Transactions on Automation Science and Engineering* 15(4): 1639–1653.
- Kang S, Wu H, Yang X, et al. (2020) Fractional-order robust model reference adaptive control of piezo-actuated active vibration isolation systems using output feedback and multi-objective optimization algorithm. *Journal of Vibration and Control* 26(1–2): 19–35.
- Lanzon A and Petersen IR (2008) Stability robustness of a feedback interconnection of systems with negative imaginary frequency response. *IEEE Transactions on Automatic Control* 53(4): 1042–1046.
- Li CX, Ding Y, Gu GY, et al. (2016a) Damping control of piezo-actuated nanopositioning stages with recursive delayed position feedback. *IEEE/ASME Transactions on Mechatronics* 22(2): 855–864.
- Li CX, Gu GY, Zhu LM, et al. (2016b) Odd-harmonic repetitive control for high-speed raster scanning of piezoactuated nanopositioning stages with hysteresis nonlinearity. *Sensors and Actuators A: Physical* 244: 95–105.
- Li J, Huang H and Morita T (2019) Stepping piezoelectric actuators with large working stroke for nano-positioning systems: a review. *Sensors and Actuators A: Physical* 292: 39–51.
- Li L, Li CX, Gu G, et al. (2017) Positive acceleration, velocity and position feedback based damping control approach for piezo-actuated nanopositioning stages. *Mechatronics* 47: 97–104.
- Ling J, Feng Z, Ming M, et al. (2019) Model reference adaptive damping control for a nanopositioning stage with load uncertainties. *Review of Scientific Instruments* 90(4): 045101.
- Ling J, Rakotondrabe M, Feng Z, et al. (2020) A robust resonant controller for high-speed scanning of nanopositioners: design and implementation. *IEEE Transactions on Control Systems Technology* 28(3): 1116–1123.
- Liu L, Tan KK, Teo CS, et al. (2012) Development of an approach toward comprehensive identification of hysteretic dynamics in piezoelectric actuators. *IEEE Transactions on Control Systems Technology* 21(5): 1834–1845.
- Liu Y, Shan J and Gabbert U (2014) Feedback/feedforward control of hysteresis-compensated piezoelectric actuators for high-speed scanning applications. *Smart Materials and Structures* 24(1): 015012.
- Lu ZQ, Shao D, Fang ZW, et al. (2020) Integrated vibration isolation and energy harvesting via a bistable piezocomposite plate. *Journal of Vibration and Control* 26(9–10): 779–789.
- Mahmood I and Moheimani SR (2009) Making a commercial atomic force microscope more accurate and faster using positive position feedback control. *Review of Scientific Instruments* 80(6): 063705.
- Namavar M and Aphale SS (2014) A modified polynomialbased controller for enhancing the positioning bandwidth of nanopositioners. *IFAC Proceedings Volumes* 47(3): 5890–5895.
- Namavar M, Fleming AJ, Aleyaasin M, et al. (2013) An analytical approach to integral resonant control of second-order systems. *IEEE/ASME Transactions on Mechatronics* 19(2): 651–659.
- Patra S and Lanzon A (2011) Stability analysis of interconnected systems with mixed negative-imaginary and small-gain properties. *IEEE Transactions on Automatic Control* 56(6): 1395–1400.

- Petersen IR (2016) Negative imaginary systems theory and applications. *Annual Reviews in Control* 42: 309–318.
- Petersen IR and Lanzon A (2010) Feedback control of negative imaginary systems. *IEEE Control Systems Magazine* 30(5): 54–72.
- Rakotondrabe M (2017) Multivariable classical prandtl–lishlinskii hysteresis modeling and compensation and sensorless control of a nonlinear 2-dof piezoactuator. *Nonlinear Dynamics* 89(1): 481–499.
- Rana M, Pota HR and Petersen IR (2016) Improvement in the imaging performance of atomic force microscopy: a survey. *IEEE Transactions on Automation Science and Engineering* 14(2): 1265–1285.
- Sabarianand DV, Karthikeyan P and Muthuramalingam T (2020) A review on control strategies for compensation of hysteresis and creep on piezoelectric actuators based micro systems. *Mechanical Systems and Signal Processing* 140: 106634.
- Salapaka SM and Salapaka MV (2008) Scanning probe microscopy. *IEEE Control Systems Magazine* 28(2): 65–83.
- San-Millan A, Russell D, Feliu V, et al. (2015) A modified positive velocity and position feedback scheme with delay compensation for improved nanopositioning performance. *Smart Materials and Structures* 24(7): 075021.
- Shahabi P, Ghafarirad H and Taghvaeipour A (2020) High-frequency robust position control of a nonlinear piezoelectric bending actuator. *Journal of Vibration and Control* 107754631990085.
- Shan J, Liu Y, Gabbert U, et al. (2016) Control system design for nano-positioning using piezoelectric actuators. *Smart Materials and Structures* 25(2): 025024.
- Skogestad S and Postlethwaite I (2007) *Multivariable Feedback Control: Analysis and Design*. New York: Wiley, Vol. 2.
- Verbaan K, van der Meulen S and Steinbuch M (2017) Broadband damping of high-precision motion stages. *Mechatronics* 41: 1–16.
- Wu Z and Xu Q (2018) Design, optimization and testing of a compact xy parallel nanopositioning stage with stacked structure. *Mechanism and Machine Theory* 126: 171–188.
- Xu Q (2017) Continuous integral terminal third-order sliding mode motion control for piezoelectric nanopositioning system. *IEEE/ASME Transactions on Mechatronics* 22(4): 1828–1838.
- Yong YK, Moheimani SOR, Kenton BJ, et al. (2012) Invited review article: high-speed flexure-guided nanopositioning: mechanical design and control issues. *Review of Scientific Instruments* 83(12): 121101.
- Yong YK, Bazaie A and Moheimani SR (2013) Video-rate lissajous-scan atomic force microscopy. *IEEE Transactions on Nanotechnology* 13(1): 85–93.
- Zhang Y, Yan P and Zhang Z (2017) Robust adaptive backstepping control for piezoelectric nano-manipulating systems. *Mechanical Systems and Signal Processing* 83: 130–148.